Fluorescence lidar observations of wildfire smoke inside cirrus: A contribution to smoke-cirrus - interaction research

Igor Veselovskii[1], Qiaoyun Hu[2], Albert Ansmann[3], Philippe Goloub[2], Thierry Podvin[2], Mikhail Korenskiy[1]

[1]*Prokhorov General Physics Institute of the Russian Academy of Sciences, Moscow, Russia.*

[2]*Univ. Lille, CNRS, UMR 8518 - LOA - Laboratoire d'Optique Atmosphérique, Lille, 59000, France*

[3]*Leibniz Institute for Tropospheric Research, Leipzig, Germany*

Correspondence: Igor Veselovskii (iveselov@hotmail.com)

Abstract

A remote sensing method, based on fluorescence lidar measurements, that allows to detect and to quantify the smoke content in upper troposphere and lower stratosphere (UTLS) is presented. The unique point of this approach is that, smoke and cirrus properties are observed in the same air volume simultaneously. In this article, we provide results of fluorescence and multiwavelength Mie-Raman lidar measurements performed at ATOLL observatory from Laboratoire d'Optique Atmosphérique, University of Lille, during strong smoke episodes in the summer and autumn seasons of 2020. The aerosol fluorescence was induced by 355 nm laser radiation and the fluorescence backscattering was measured in a single spectral channel, centered at 466 nm and having 44 nm width. To estimate smoke particle properties, such as number, surface area and volume concentration, the conversion factors, which link the fluorescence backscattering and the smoke microphysical properties, are derived from the synergy of multiwavelength Mie-Raman and fluorescence lidar observations. Based on two case studies, we demonstrate that the fluorescence lidar technique provides the possibility to estimate the smoke surface area concentration within freshly formed cirrus layers. This value was used in smoke INP parameterization scheme to predict ice crystal number concentrations in cirrus generation cells.

Introduction

Aerosol particles in the upper tropospheric and lower stratospheric (UTLS) height regime play an important role in processes of heterogeneous ice formation, however our current understanding of these processes is still insufficient for a trustworthy implementation in numerical

32 weather and climate prediction models. The ability of aerosol particles to act as ice nucleating

33 particles (INP) depends on meteorological factors such as temperature and ice supersaturation (as

34 a function of vertical velocity), as well as on the aerosol type in the layer in which cirrus developed

35 (Kanji et al., 2017). Heterogeneous ice nucleation initiated by insoluble inorganic materials such

36 as mineral dust has been studied since a long time (e.g., DeMott et al 2010, 2015; Hoose and

37 Möhler, 2012; Murray et al., 2012; Boose et al., 2016; Schrod et al., 2017; Ansmann et al. 2019b),

38 while the potential of omnipresent organic particles, especially of frequently occurring aged, long-

39 range-transported wildfire smoke particles, to act as INP is less well explored and thus not well

40 understood (Knopf et al., 2018). Wildfire smoke can reach the lower stratosphere via pyro-

41 cumulonimbus (pyroCb) convection (Fromm et al., 2010; Peterson et al., 2018, 2021; Hu et al.,

42 2019; Khaykin et al., 2020) or via self-lifting processes (Boers et al., 2010,Ohneiser et al., 2021).

43 It is widely assumed that the ability of smoke particles to serve as INP mainly depends on the

44 organic material (OM) in the shell of the coated smoke particles (Knopf et al., 2018), but may also

45 depend on mineral components in the smoke particles (Jahl et al., 2021). The ice nucleation

46 efficiency may increase with increasing duration of the long-range transport as Jahl et al. (2021)

47 suggested. Disregarding the progress made in this atmospheric research field during the last years,

48 the link between ice nucleation efficiency and the smoke particle chemical and morphological

49 properties is still largely unresolved (China et al., 2017; Knopf et al., 2018).

50   To contribute to the field of smoke-cirrus-interaction research, we present a laser remote

51 sensing method that allows us simultaneously to detect and quantify the smoke particles amount

52 inside of cirrus layers together with cirrus properties and to provide INP estimates in regions close

53 to the cloud top where ice formation usually begins. The unique point of our approach is that, for

54 the first time, smoke and cirrus properties are observed in the same air volume simultaneously.

55 Recently, a first attempt (closure study) was performed to investigate the smoke impact on High

56 Arctic cirrus formation (Engelmann et al. 2021). However, the aerosol measurements had to be

57 performed outside the clouds layers, and then an assumption was needed that the estimated aerosol

58 (and estimated INP) concentration levels also hold inside the cirrus layers. Now, we propose a

59 method to directly determine INP-relevant smoke parameters inside the cirrus layer during ice

60 nucleation events. This also offers the opportunity to illuminate whether an INP reservoir can be

61 depleted in cirrus evolution processes or not. Furthermore, this new lidar detection method permits

62 a clear discrimination between, e.g., smoke and mineral dust INPs.

63   Multiwavelength Mie-Raman lidars or High Spectral Resolution lidars (HSRL) are

64   favorable instruments to provide the vertical profiles of the physical properties of tropospheric

65   aerosol particles. In particular, the inversion of the so-called 3β+2α lidar observations, based on

66   the measurement of height profiles of three aerosol backscatter coefficients at 355, 532, and 1064

67   nm and two extinction coefficients at 355 and 532 nm, allows us to estimate smoke microphysical

68   properties (Müller et al., 1999, 2005; Veselovskii et al., 2002, 2015). However, the aerosol content

69   in UTLS height range can be low, so that particle extinction coefficients cannot be determined

70   with sufficient accuracy and are thus not available in the lidar inversion data analysis. To resolve

71   this issue Ansmann et al. (2019a, 2021) used the synergy of polarization lidar measurements and

72   Aerosol Robotic Network (AERONET) sunphotometer observations (Holben et al., 1998) to

73   derive conversion factors (to convert backscatter coefficients into microphysical particle

74   properties) and to estimate INP concentrations for dust and smoke aerosols with the retrieved

75   aerosol surface area concentration as aerosol input.

76   Dust particles are very efficient ice nuclei in contrast to wildfire smoke particles. In this

77   context, the question arises: How can we unambiguously discriminate smoke from dust particles?

78   This is realized by integrating a fluorescence channel into a multiwavelength aerosol lidar

79   (Reichardt et al., 2017; Richardson et al., 2019; Veselovskii et al., 2020; 2021). The fluorescence

80   capacity of smoke (ratio of fluorescence backscattering to the overall aerosol backscattering),

81   significantly exceeds corresponding values for other types of aerosol, such as dust or

82   anthropogenic particles (Veselovskii et al., 2020; 2021), and thus allows us to discriminate smoke

83   from other aerosol types. The fluorescence technique provides therefore the unique opportunity to

84   monitor ice formation in well identified wildfire smoke layers, and thus to create a good basis for

85   long-term investigations of smoke cirrus interaction.

86   In this article, we present results of fluorescence and multiwavelength Mie-Raman lidar

87   measurements performed at the ATOLL (ATmospheric Observation at liLLe) of the Laboratoire

88   d'Optique Atmosphérique, University of Lille, during strong smoke episodes in the summer and

89   autumn seasons of 2020. The results demonstrate that the fluorescence lidar is capable to monitor

90   the smoke in the UTLS height range and inside the cirrus clouds formed at or below the tropopause.

91   We start with a brief description of the experimental setup in Sect.2. In the first part of the result

92   section (Sect.3.1 and 3.2), it is explained how smoke optical properties can be quantified by using

93   fluorescence backscattering information and how we can estimate smoke microphysical properties

94   (volume, surface area, and number concentration) from measured fluorescence backscatter

95   coefficients. In this approach, multiwavelength Mie-Raman aerosol lidar observations are used in

96   addition. The retrieved values of the smoke particle surface area concentration are then the aerosol

97   input in the smoke INP estimation. A case study is discussed in Sect.3.2. Two case studies are then

98   presented in Sect.3.3 to demonstrate the capability of a fluorescence lidar to monitor ice formation

99   in extended smoke layers and to provide detailed information on aerosol microphysical properties

100   and smoke-relate INP concentration levels.

101

2. Experimental setup

103   The multiwavelength Mie-Raman lidar LILAS (LIlle Lidar AtmosphereS) is based on a

104   tripled Nd:YAG laser with a 20 Hz repetition rate and pulse energy of 70 mJ at 355 nm.

105   Backscattered light is collected by a 40 cm aperture Newtonian telescope and the lidar signals are

106   digitized with Licel transient recorders of 7.5 m range resolution, allowing simultaneous detection

107   in the analog and photon counting mode. The system is designed for simultaneous detection of

108   elastic and Raman backscattering, allowing the so called $3\beta+2\alpha+3\delta$ data configuration, including

109   three particle backscattering (β_{355}, β_{532}, β_{1064}), two extinction (α_{355}, α_{532}) coefficients along with

110   three particle depolarization ratios (δ_{355}, δ_{532}, δ_{1064}). The particle depolarization ratio, determined

111   as a ratio of cross- and co-polarized components of the particle backscattering coefficient, was

112   calculated and calibrated in the same way as described in Freudenthaler et al. (2009). The aerosol

113   extinction and backscattering coefficients at 355 and 532 nm were calculated from Mie-Raman

114   observations (Ansmann et al., 1992), while β_{1064} was derived by the Klett method (Fernald, 1984;

115   Klett, 1985). Additional information about atmospheric parameters was available from radiosonde

116   measurements performed at Herstmonceux (UK) and Beauvecchain (Belgium) stations, located

117   160 km and 80 km away from the observation site respectively.

118   This lidar system is also capable to perform aerosol fluorescence measurements. A part of

119   the fluorescence spectrum is selected by a wideband interference filter of 44 nm width centered at

120   466 nm (Veselovskii et al., 2020; 2021). The strong sunlight background at daytime restricts the

121   fluorescence observations to nighttime hours. To characterize the fluorescence properties of

122   aerosol, the fluorescence backscattering coefficient β_F is calculated from the ratio of fluorescence

123   and nitrogen Raman backscatters, as described in Veselovskii et al. (2020). This approach allows

124   to evaluate the absolute values of β_F, if the relative sensitivity of the channels is calibrated and the

125   nitrogen Raman scattering differential cross section σ_R is known. In our research we used

126     $\sigma_R=2.744*10^{-30}$ cm^{2}sr^{-1} at 355 nm from Venable et al. (2011). All β_F profiles presented in this

127   work were smoothed with the Savitzky – Golay method, using second order polynomial with 21

128   points in the window. The efficiency of fluorescence backscattering with respect to elastic

129   backscattering β_{532} is characterized by the fluorescence capacity $G_F = \dfrac{\beta_F}{\beta_{532}}$.

130   For most of atmospheric particles β_F is proportional to the volume of dry matter, while dependence

131   of β_{532} on particle size is more complicated. As a result, G_F depends not only on aerosol type, but

132   also on particle size and the relative humidity RH. Uncertainty of β_F calculation depends on the

133   chosen value of σ_R and on relative transmission of optical elements in fluorescence and nitrogen

134   channels. These system parameters do not change with time. The relative sensitivity of PMTs,

135   however, may change. Regular calibration of the channels relative sensitivity (Veselovskii et al.,

136   2020), demonstrates that corresponding uncertainty can be up to 10%. At high altitudes the

137   statistical uncertainty becomes predominant. We recall also, that only a part of the fluorescence

138   spectra was selected by the interference filter in the receiver, so provided values of β_F and G_F are

139   specific for the filter used. Analyzing the fluorescence measurements we should keep in mind, that

140   the sensitivity of this technique can be limited by the fluorescence of optics in the lidar receiver.

141   The minimal value of G_F, which we measured during observation in cloudy conditions in the lower

142   troposphere was about 2×10^{-8}. Thus, at least, in the measurements with G_F above this value, the

143   contribution of optics fluorescence can be ignored.

144

145   **3. Results of the measurements**

146   *3.1. Observation of smoke particles in UTLS*

147   Smoke particles produced by intensive fires and transported across the Atlantic are

148   regularly observed in the UTLS height range over Europe (Müller et al., 2005; Hu et al., 2019;

149   Baars et al., 2019, 2021). One of such events, observed over Lille in the night of 4-5 November

150   2020, is shown in Fig.1. The figure provides height – time displays of the range corrected lidar

151   signal and the volume depolarization ratio at 1064 nm together with the fluorescence

152   backscattering coefficient. A narrow smoke layer occurred in the upper troposphere in the period

153   from 23:00 – 06:00 UTC. The smoke was detected at heights above 12 km after midnight. The

154   particles caused a low volume depolarization ratio (<5%) at 1064 nm and strong fluorescence

155   backscattering (β_F>1.2×10^{-4} Mm^{-1}sr^{-1}). The backward trajectory analysis indicated that the aerosol

156   layer was transported over the Atlantic and contained products of North American wild fires.

157   Vertical profiles of aerosol β_{532} and fluorescence β_F backscattering coefficients for the

158   period from 02:00 - 05:30 UTC are shown in Fig.2a. The fluorescence capacity G_F in the center of

159   smoke layer (not shown) was about 4.5×10^{-4}. The depolarization ratio of aged smoke in the UTLS

160   height range usually shows a strong spectral dependence (Haarig et al., 2018; Hu et al., 2019). For

161   the case presented in Fig.2a the particle depolarization ratio in the center of the smoke layer

162   decreased from 16±4% at 355 nm (δ_{355}) to 4±1% at 1064 (δ_{1064}). The tropopause height H_{tr} was at

163   about 13000 m, thus the main part of the smoke layer was below the tropopause. By the end of day

164   the smoke layer became weaker (β_F<0.3×10^{-4} Mm^{-1}sr^{-1}) and ascended up to 14500 m, which is

165   above the tropopause. The corresponding vertical profiles of β_{532} and β_F are shown in Fig.2b. The

166   fluorescence capacity in the center of the layer is about 4.5×10^{-4}, which is close to the value

167   observed during 02:00 - 05:30 UTC period.

168   An important advantages of the fluorescence lidar technique is the ability to monitor

169   smoke particles inside cirrus clouds. The results of smoke observations in the presence of ice

170   clouds are shown in Fig.3. Cirrus clouds occurred during the whole night in the height range from

171   6.0 km – 10.0 km. To quantify the fluorescence backscattering inside the cloud (which was rather

172   weak in this case), the lidar signals were averaged over the full 18:00 – 06:00 UTC time interval

173   in Fig.3a. The fluorescence backscatter coefficient shown in Fig.3c decreased from β_F=0.015×10^{-4}

174   Mm^{-1}sr^{-1} at 5000 m (near the cloud base) to a minimum value of 0.01×10^{-4} Mm^{-1}sr^{-1} at 7000 m

175   inside the cirrus layer. Above the tropopause the fluorescence backscattering increased strongly

176   and reached the maximum (about 0.3 ×10^{-4} Mm^{-1}sr^{-1}) in 11000 m -13000 m height.

177   The analysis of fluorescence measurements performed during strong smoke episodes in the

178   summer and autumn of 2020, when smoke layers from North American fires frequently reached

179   Europe, demonstrates that the fluorescence capacity varied within the range of 2.5×10^{-4} to 4.5×10^{-4}

180   . The variations are a function of smoke composition, relative humidity and particle size.

181   However, in the upper troposphere, where relative humidity is low, G_F was normally close to

182   4.5×10^{-4}. This relatively low range of G_F variations allows the estimation of the backscattering

183   coefficient attributed to the smoke particles from fluorescence measurements as:

184     $$\beta_{532}^{s} = \frac{\beta_F}{G_F}.$$ (1)

185   Fig.3d shows the smoke backscattering coefficient β_{532}^{s}, calculated from β_F for G_F=4.5×10⁻

186   ⁴, together with β_{532}. The dynamical range of β_{532} variations is high. To make smoke backscattering

187   visible above H_{Tr}, β_{532} is plotted in expanded scale in Fig.3d. The β_{532}^{s} values, though being

188   strongly oscillating above the tropopause, match the β_{532} indicating that the smoke contribution to

189   backscattering was predominant.

190

191   **3.2. Estimation of smoke particles content based on fluorescence measurements**

192   The possibility to detect fluorescence backscattering inside the cirrus clouds reveals also

193   the opportunity for a quantitative characterization of the smoke content. This can be realized by a

194   synergistic use of fluorescence and multiwavelength Mie – Raman lidar observations. The flow

195   chart, summarizing the main steps of this procedure, is presented in **Appendix 1**. For the smoke

196   layers with sufficient optical depth, the number N, surface area S and volume V concentrations can

197   be evaluated, by inverting the 3β+2α observations consisting of three backscatter coefficients

198   (355, 532, 1064 nm) and two extinction coefficients (355, 532 nm) (Müller et al., 1999;

199   Veselovskii et al., 2002; Pérez-Ramírez et al., 2013). The conversion factors C_N, C_S, C_V, introduced

200   as

201    $$C_N = \frac{N}{\beta_F}, \; C_S = \frac{S}{\beta_F}, \; C_V = \frac{V}{\beta_F}, \tag{3}$$

202   allow the estimation of smoke particle concentration inside the clouds from fluorescence

203   backscattering, assuming that smoke contribution to the fluorescence is predominant. Moreover,

204   it allows estimation of the particles concentration in weak smoke layers in UTLS, where 3β+2α

205   observations are normally not available.

206   On 23-24 June 2020, a strong smoke layer was observed in 4500 – 5500 m height during

207   the whole night (Fig.4). The vertical profiles of the aerosol backscattering and extinction

208   coefficients (3β+2α) are shown in Fig.5a, while the particle depolarization ratios δ_{355}, δ_{532}, δ_{1064}

209   and the lidar ratios at 355 nm and 532 nm (LR_{355}, LR_{532}) are presented in Fig.5b. The depolarization

210   ratio decreases with wavelength from 9±1.5% at 355 nm to 1.5±0.3% at 1064 nm and the lidar

211   ratio at 532 nm significantly exceeds corresponding value at 355 nm (80±12 sr and 50±7.5 sr

212   respectively), which is typical for aged smoke (Müller et al., 2005). The multiwavelength

213   observations were inverted to determine the particle effective radius r_{eff}, number, surface area and

volume concentrations for seven height bins inside the smoke layer. The effective radius r_{eff} in Fig.5c increases through the layer from 0.15 μm to 0.2 μm simultaneously with the increase of the fluorescence capacity G_F from 2.8×10^{-4} to 3.6×10^{-4}. Retrieved values of N, S, V were used for the calculation of the conversion factors (Eq. 3) for each height bin. In the center of the smoke layer (at 4.9 km) the factors are: $C_N = 88 \times 10^4 \dfrac{cm^{-3}}{Mm^{-1}sr^{-1}}$, $C_S = 35 \times 10^4 \dfrac{\mu m^2 cm^{-3}}{Mm^{-1}sr^{-1}}$, and $C_V = 2.4 \times 10^4 \dfrac{\mu m^3 cm^{-3}}{Mm^{-1}sr^{-1}}$.

Thus, when β_F is given in $Mm^{-1}sr^{-1}$, the calculated values of N, S, and V are given in cm^{-3}, $\mu m^2 cm^{-3}$ and $\mu m^3 cm^{-3}$ respectively. Fluorescence backscattering is proportional to the particle volume concentration, so C_V is not sensitive to the effective radius variation. The conversion factors C_N and C_S, on the contrary, depend on the particle size. Fig.5d shows the profiles of N, S, V obtained by inversion of $3\beta+2\alpha$ observations (symbols) together with corresponding values (N^S, S^S, V^S) obtained from β_F, using the mean conversion factors for seven height bins considered. The volume concentrations V and V^S agree well for all seven height bins. For the surface area concentrations the agreement is still good, but for N and N^S the difference is up to 30%. We need to emphasize, that the conversion factors presented are specific for our lidar system (for the interference filter installed in fluorescence channel). It is worthwhile to mention that the ratio V/α_{532} of the volume concentration V in Fig.5d to the extinction coefficient α at 532 nm in Fig.5a, as well as the ratio S/α_{532}, are very close to respective extinction-to-volume and extinction-to-surface-area-concentration conversion factors presented for aged wildfire smoke by Ansmann et al. (2021).

The conversion factors depend on the smoke composition. To estimate the variation range of C_N, C_S, C_V, several smoke episodes were analyzed and corresponding results are presented in Table 1. The table provides the fluorescence capacity G_F and the conversion factors at the heights, where $3\beta+2\alpha$ data could be calculated. Mean values of $<C_N>$, $<C_S>$, $<C_V>$ derived for these episodes and corresponding standard deviations are:

$$<C_N>=(61\pm32)\times10^4 \frac{cm^{-3}}{Mm^{-1}sr^{-1}} \; ; <C_S>=(28\pm6.4)\times10^4 \frac{\mu m^2 cm^{-3}}{Mm^{-1}sr^{-1}} \; ; <C_V>=(2.2\pm0.2)\times10^4 \frac{\mu m^3 cm^{-3}}{Mm^{-1}sr^{-1}} \quad (4)$$

Table 1 shows also the volume and surface area concentrations of the smoke particles obtained from the inversion of $3\beta+2\alpha$ observations (V, S) and calculated from β_F (V^S, S^S) using the conversion factors in Eq. (4). Standard deviations of V^S and S^S from corresponding values of $V_{3\beta+2\alpha}$ and $S_{3\beta+2\alpha}$ are 10% and 25% respectively.

242   The mean conversion factors in Eq. (4) are now used to estimate the smoke microphysical
243 properties inside the cloud, assuming in addition that the predominant contribution to the
244 fluorescence is provided by the smoke. Table 2 summarizes the number, surface area, and volume
245 concentrations of smoke particles inside the ice clouds, estimated from fluorescence measurements
246 for four episodes considered in this paper. On September 12-13, 2020, the smoke layer with high
247 fluorescence and low depolarization ratio at 1064 nm (below 4%) was observed during the whole
248 night inside the 2.0 km − 5.0 km height range. The cirrus cloud occurred above 11000 m also
249 during the whole night. Fig.6a presents vertical profiles of the aerosol β_{532} and fluorescence β_F
250 backscattering coefficients. Fluorescence backscattering shows a maximum at 3.5 km, but it is
251 detected even inside the cloud. The smoke backscattering coefficient β_{532}^{s}, computed from β_F for

252 $G_F=3.6\times10^{-4}$ agrees well with β_{532} inside the 2.0 − 10.0 km height range (Fig.6b). The height profile
253 of the surface area concentration of the smoke particles S^S, calculated from β_F using the respective
254 conversion factor in Eq. (4), is shown in Fig.6c. In the smoke layer, S^S is up to 60 μm^2/cm^3, while
255 in the center of the cloud in 12 km − 13 km height the average value of S^S is 1.6±0.4 μm^2/cm^3.
256 Corresponding values of number and volume concentrations in the cloud center are 3.5±1.8 cm^{-3}
257 and 0.13±0.013 μm^3/cm^3.

258   The temperature in the cloud ranged from about -50°C to almost -70°C and was -68°C at
259 cirrus top in Fig.6b where ice nucleation usually starts. We applied the immersion freezing INP
260 parameterization of Knopf and Alpert (2013) for Leonardite (a standard humic acid surrogate
261 material) and assume that this humic compound represents the amorphous organic coating of
262 smoke particles. The INP parameterization for smoke particles is summarized for lidar applications
263 in Ansmann et al. (2021). The selected parameterization allows the estimation of the INP
264 concentration as a function of ambient air temperature (freezing temperature), ice supersaturation,
265 particle surface area, and time period for which a certain level of ice supersaturation is given. We
266 simply assume a constant ice supersaturation of around 1.45 during a time period of 600 s (upwind
267 phase of a typical gravity wave in the upper troposphere). The temperature at cirrus top height is
268 set to -68°C and the aerosol surface area concentration to 2.0 μm^2/cm^3 as indicated in Fig.6c. The
269 obtained INP concentrations of 1-10 L^{-1} for these meteorological and aerosol environmental
270 conditions can be regarded as the predicted number concentration of ice crystals nucleated in the
271 cirrus top region. Ice crystal number concentration of 1-10 L^{-1} are typical values in cirrus layers
272 when heterogeneous ice nucleation dominates (typical values of INP concentrations and

273 supersaturation are discussed e.g. in Sullivan et al, (2016), Ansmann et al. (2019; 2021),

274 Engelmann et al. (2021)). It should be mentioned that the required very high ice supersaturation

275 levels of close to 1.5 (ice supersaturation of 1.1-1.2 is sufficient in case of mineral dust particles)

276 are still lower than the threshold supersaturation level of >1.5 at which homogeneous freezing

277 starts to dominate. At low updraft velocities around 10-25 cm/s, as usually given in gravity waves

278 in the upper troposphere (Barahona et al., 2017), heterogeneous ice nucleation very likely

279 dominates the ice production when cirrus evolves in detected aerosol layers.

280

281 ### 3.3. Ice formation inside the smoke layers.

282 During September 2020 we observed several episodes with ice cloud formation inside of

283 smoke layers. One of such episodes occurred on 11-12 September 2020 and is shown in Fig.7. The

284 height – time display of the fluorescence backscattering coefficient reveals the smoke layer in the

285 5.0 - 10.0 km height range. Inside this layer, we can observe a short time interval of 15 minutes

286 with a strongly increased depolarization ratio around 10.5 km height (red spots), indicating ice

287 cloud formation. Fig.8 shows vertical profiles of the aerosol backscattering coefficients β_{355}, β_{532},

288 and β_{1064} as well the particle depolarization ratios δ_{355}, δ_{532}, and δ_{1064} for two temporal intervals.

289 The first interval (23:00 – 00:30 UTC) is prior to ice cloud formation and the second one (01:20 –

290 01:45 UTC) covers ice occurrence period. The depolarization ratios at all three wavelengths were

291 < 5% below 6 km height. Above that height δ_{355} significantly increased reaching the value of 10%

292 at 7 km (Fig.8b), which is indicative of a change of the particle shape (from spherical to irregular

293 shape). The fluorescence capacity also changed with height, being about $G_F=4.5\times10^{-4}$ at 5.5 km

294 and it decreases to 3.5×10^{-4} by 8 km. The profile of β_{532}^{s} shown in Fig.8c is calculated assuming

295 $G_F=4.0\times10^{-4}$ and it matches well the profile of β_{532} for the whole height range. The aerosol layer

296 at 10.5 km is thus a pure smoke layer. Ice formation at 10.5 km (Fig.8d-f) leads to a significant

297 increase of β_{532} while β_{532}^{s} (or the respective fluorescence backscatter coefficient β_F) remains low

298 and at the same level as observed below the cirrus layer, i.e., below 10 km height. The

299 depolarization ratios at all three wavelengths increases to typical cirrus values around 40%. The

300 temperature at 10.5 km is about -50 °C, and the surface area concentration of the smoke particles

301 inside the cloud, estimated from β_F, is about 10 $\mu m^2/cm^3$ (see Fig.8f, thin blue line). For these

302 temperature and aerosol conditions we yield smoke INP concentrations of 1-10 L^{-1} for ice

303 supersaturation values even below 1.4 (1.38-1.4) and updraft duration of 600 s. When comparing

304 Fig.8c and 8f at cirrus level it seems to be that ice nucleation on the smoke particles widely

305 depleted the smoke INP reservoir.

306 Another case of ice formation in the smoke layer was observed on 17-18 September 2020.

307 Strong smoke layers occurred in the 5.0 km – 9.0 km height range as shown in Fig.9. During the

308 period from 22:30 – 00:00 UTC, the depolarization increased at 8.5 km height, indicating ice

309 formation. Vertical profiles of the particle parameters prior and during ice formation are shown in

310 Fig.10. The β^{s}_{532} calculated for G_F=3.5×10^{-4} matches well with β_{532} below 6.9 km and above 8.0

311 km (Fig.10c), but inside the 7.0 km – 8.0 km height range $\beta_{532} > \beta^{s}_{532}$, meaning that G_F was

312 decreased. The depolarization ratio in the 7.0 km – 8.0 km height range shows some enhancement

313 (Fig.10b): in particular, δ_{532} increased from 10% to 12%. Cloud formation at 8.5 km (Fig.10d) led

314 to a significantly smaller increase of the depolarization ratio, compared to the case on 11-12

315 September. Prior to the cloud formation the values of δ_{1064}, δ_{532}, and δ_{355} at 8.5 km were of 3%,

316 10%, and 13% respectively (Fig.10b) and in the cloud corresponding depolarization ratios increase

317 up to 9%, 15%, 20%. The reason is probably that the signal averaging period from 22:45 to 23:45

318 UTC includes cloud-free section. Three gravity waves obviously crossed the lidar field site and

319 triggered ice nucleation just before 23 UTC, 15-30 minutes after 23 UTC, and around mid night

320 (00:00 UTC). The temperature at cloud top at about 8.5-8.6 km height was close to -35°C. For this

321 high temperature and the high particle surface area concentration of 200 μm^2/cm^3 (see Fig.10d,

322 thin blue line) we yield smoke INP concentrations of 1-10 L^{-1} for a relatively low ice

323 supersaturation of 1.30-1.33 and an updraft period of 600 s. Again, a depletion of the INP reservoir

324 is visible after formation of the cirrus layer (see Figs.6c and 6d around and above 8.5 km height).

325

326 **Conclusion**

327 The operation of a fluorescence channel in the LILAS lidar during strong smoke events in

328 the summer and autumn seasons of 2020 has demonstrated the ability of the fluorescence lidar

329 technique to discriminate ice from smoke particles in atmospheric layers in the UTLS height range

330 in large detail. The fluorescence capacity G_F of smoke particles during this period varied within a

331 relatively small range: 2.5-4.5×10^{-4}, thus the use of the mean value of G_F allows to estimate the

332 contribution of smoke to the total particle backscattering coefficient. The fluorescence lidar

333 technique makes it possible to estimate smoke parameters, such as number, surface area and
334 volume concentration in UTLS height range in a quantitative way by applying conversion factors
335 (C_N, C_S, C_V) which link the fluorescence backscattering and the smoke microphysical properties.
336 These factors, derived from the synergy of multiwavelength Mie-Raman and fluorescence lidar
337 observations, show some variation from episode to episode, however, the use of mean values
338 $<C_N>$, $<C_S>$, $<C_V>$ allows estimation of smoke properties in UTLS height regime with reasonable
339 accuracy. Based on two case studies, we demonstrated that the fluorescence lidar technique
340 provides the unique possibility to characterize the smoke particles and their amount inside cirrus
341 cloud layers. The smoke input parameter (surface area concentration) in smoke INP
342 parameterization schemes that are used to predict ice crystal number concentrations in cirrus
343 generation cells, can now be estimated within freshly formed cirrus layers.

344 The smoke parameters such as fluorescence capacity and conversion factors were derived
345 from observations of aged wildfire smoke, transported over Atlantic in 2020. However, smoke
346 composition, depends on many factors, such as burning materials type, flame temperature and
347 environmental conditions, thus the smoke fluorescence properties may also vary. Hence, it is
348 important to perform the measurements for different locations and seasons. The fluorescence
349 backscattering in UTLS height range is quite weak, so to perform measurements with higher
350 temporal resolution more powerful lidar systems are needed. A dedicated high power Lidar, LIFE
351 (Laser Induced Fluorescence Explorer), will be designed and operated at ATOLL, in the frame of
352 OBS4CLIM/ACTRIS-France .

353

354

355 **Acknowledgement**

356 We acknowledge funding from the CaPPA project funded by the ANR through the PIA under
357 contract ANR-11-LABX-0005-01, the "Hauts de France" Regional Council (project CLIMIBIO)
358 and the European Regional Development Fund (FEDER). Development of algorithm for analysis
359 of fluorescence observations was supported by Russian Science Foundation (project 21-17-
360 00114). ESA/QA4EO program is greatly acknowledged for his support to the observation activity
361 at LOA.

362

References

Ansmann, A., Riebesell, M., Wandinger, U., Weitkamp, C., Voss, E., Lahmann, W., and Michaelis, W.: Combined Raman elastic-backscatter lidar for vertical profiling of moisture, aerosols extinction, backscatter, and lidar ratio, Appl.Phys.B, *55*, 18-28, 1992.

Ansmann, A., Baars, H., Chudnovsky, A., Mattis, I., Veselovskii, I., Haarig, M., Seifert, P., Engelmann, R., and Wandinger, U.: Extreme levels of Canadian wildfire smoke in the stratosphere over central Europe on 21–22 August 2017, Atmos. Chem. Phys., 18, 11831–11845, 2018. https://doi.org/10.5194/acp-18-11831-2018.

Ansmann, A., Mamouri, R.-E., Hofer, J., Baars, H., Althausen, D., and Abdullaev, S. F.: Dust mass, cloud condensation nuclei, and ice-nucleating particle profiling with polarization lidar: updated POLIPHON conversion factors from global AERONET analysis, Atmos. Meas. Tech., 12, 4849–4865, https://doi.org/10.5194/amt-12-4849-2019, 2019a.

Ansmann, A., Mamouri, R.-E., Bühl, J., Seifert, P., Engelmann, R., Hofer, J., Nisantzi, A., Atkinson, J. D., Kanji, Z. A., Sierau, B., Vrekoussis, M., and Sciare, J.: Ice-nucleating particle versus ice crystal number concentrationin altocumulus and cirrus layers embedded in Saharan dust:a closure study, Atmos. Chem. Phys., 19, 15087–15115, https://doi.org/10.5194/acp-19-15087-2019, 2019b.

Ansmann, A., Ohneiser, K., Mamouri, R.-E., Veselovskii, I., Knopf, D. A., Baars, H., Engelmann, R., Foth, A., Jimenez, C., Seifert, P., and Barja, B.: Tropospheric and stratospheric wildfire smoke profiling with lidar: Mass, surface area, CCN and INP retrieval, Atmos. Chem. Phys., 21, 9779–9807, 2021. https://doi.org/10.5194/acp-21-9779-2021.

Baars, H., Ansmann, A., Ohneiser, K., Haarig, M., Engelmann, R., Althausen, D., Hanssen, I., Gausa, M., Pietruczuk, A., Szkop, A., Stachlewska, I. S., Wang, D., Reichardt, J., Skupin, A., Mattis, I., Trickl, T., Vogelmann, H., Navas-Guzmán, F., Haefele, A., Acheson, K., Ruth, A. A., Tatarov, B., Müller, D., Hu, Q., Podvin, T., Goloub, P., Veselovskii, I., Pietras, C., Haeffelin, M., Fréville, P., Sicard, M., Comerón, A., Fernández García, A. J., Molero Menéndez, F., Córdoba-Jabonero, C., Guerrero-Rascado, J. L., Alados-Arboledas, L., Bortoli, D., Costa, M. J., Dionisi, D., Liberti, G. L., Wang, X., Sannino, A., Papagiannopoulos, N., Boselli, A., Mona, L., D'Amico, G., Romano, S., Perrone, M. R., Belegante, L., Nicolae, D., Grigorov, I., Gialitaki, A., Amiridis, V., Soupiona, O., Papayannis, A., Mamouri, R.-E., Nisantzi, A., Heese, B., Hofer, J., Schechner, Y. Y., Wandinger, U., and Pappalardo, G.: The

394   unprecedented 2017–2018 stratospheric smoke event: decay phase and aerosol properties

395   observed with the EARLINET, Atmos. Chem. Phys., 19, 15183–15198,

396   https://doi.org/10.5194/acp-19-15183-2019, 2019.

397   Baars, H., Radenz, M., Floutsi, A. A., Engelmann, R., Althausen, D., Heese, B., Ansmann, A.,

398   Flament, T., Dabas, A., Trapon, D., Reitebuch, O., Bley, S., and Wandinger, U.: Californian

399   wildfire smoke over Europe: A first example of the aerosol observing capabilities of Aeolus

400   compared to ground-based lidar. Geophysical Research Letters, 48, e2020GL092194.

401   https://doi.org/10.1029/2020GL092194, 2021.

402   Barahona, D., Molod, A., and Kalesse, H.: Direct estimation of the global distribution of vertical

403   velocity within cirrus clouds, Sci. Rep., 7, 20 6840, https://doi.org/10.1038/s41598-017-07038-

404   6, 2017.

405   Boose, Y., Sierau, B., Garcia, M. I., Rodriguez, S., Alastuey, A., Linke, C., Schnaiter, M.,

406   Kupiszewski, P., Kanji, Z. A., and Lohmann, U.: Ice nucleating particles in the Saharan Air

407   Layer, Atmos. Chem. Phys., 16, 9067-9087, https://doi.org/10.5194/acp-16-9067-2016, 2016.

408   China, S., Alpert, P. A., Zhang, B., Schum, S., Dzepina, K., Wright, K., Owen, R. C., Fialho, P.,

409   Mazzoleni, L. R., Mazzoleni, C., and Knopf, D. A.: Ice cloud formation potential by free

410   tropospheric particles from long-range transport over the Northern Atlantic Ocean, J. Geophys.

411   Res.-Atmos., 122, 3065–3079, https://doi.org/10.1002/2016JD025817, 2017.

412   DeMott, P. J., Prenni, A. J., Liu, X., Kreidenweis, S. M., Petters, M. D., Twohy, C. H., Richardson,

413   M. S., Eidhammer, T., and Rogers, D. C.: Predicting global atmospheric ice nuclei distributions

414   and their impacts on climate, Proc. Natl. Acad. Sci. USA, 107, 11217–11222,

415   doi:10.1073/pnas.0910818107, 2010.

416   DeMott, P. J., Prenni, A. J., McMeeking, G. R., Sullivan, R. C., Petters, M. D., Tobo, Y., Niemand,

417   M., Möhler, O., Snider, J. R., Wang, Z., and Kreidenweis, S. M.: Integrating laboratory and

418   field data to quantify the immersion freezing ice nucleation activity of mineral dust particles,

419   Atmos. Chem. Phys., 15, 393–409, doi:10.5194/acp-15-393-2015, 2015.

420   Engelmann, R., Ansmann, A., Ohneiser, K., Griesche, H., Radenz, M., Hofer, J., Althausen, D.,

421   Dahlke, S., Maturilli, M., Veselovskii, I., Jimenez, C., Wiesen, R., Baars, H., Bühl, J., Gebauer,

422   H., Haarig, M., Seifert, P., Wandinger, U., and Macke, A.: Wildfire smoke, Arctic haze, and

423   aerosol effects on mixed-phase and cirrus clouds over the North Pole region during MOSAiC:

an introduction, Atmos. Chem. Phys., 21, 13397–13423, https://doi.org/10.5194/acp-21-13397-2021, 2021.

Fernald, F. G.: Analysis of atmospheric lidar observations: some comments, Appl. Opt., 23, 652–653, doi.org/10.1364/AO.23.000652, 1984.

Freudenthaler,V., Esselborn, M.,Wiegner, M.,Heese, B., Tesche, M. and co-authors: Depolarization ratio profiling at severalwavelengths in pure Saharan dust during SAMUM 2006, *Tellus* 61B, 165–179, 2009.

Fromm, M., Lindsey, D. T., Servranckx, R., Yue, G., Trickl, T., Sica, R., Doucet, P., and Godin-Beekmann, S. E.: The untold story of pyrocumulonimbus, B. Am. Meteorol. Soc., 91, 1193–1209, https://doi.org/10.1175/2010bams3004.1, 2010.

Grawe, S., Augustin-Bauditz, S., Hartmann, S., Hellner, L., Pettersson, J. B. C., Prager, A., Stratmann, F., and Wex, H.: The immersion freezing behavior of ash particles from wood and brown coal burning, Atmospheric Chemistry and Physics, 16, 13 911–13 928, 2016. https://doi.org/10.5194/acp-16-13911-2016.

Haarig, M., Ansmann, A., Baars, H., Jimenez, C., Veselovskii, I., Engelmann, R., and Althausen, D.: Depolarization and lidar ratios at 355, 532, and 1064 nm and microphysical properties of aged tropospheric and stratospheric Canadian wildfire smoke, Atmos. Chem. Phys., 18, 11847-11861, https://doi.org/10.5194/acp-18-11847-2018, 2018.

Holben, B. N., Eck, T. F., Slutsker, I., Tanré, D., Buis, J. P., Setzer, A., Vermote, E., Reagan, J. A., Kaufman, Y. J., Nakajima, T., Lavenu, F.,Jankowiak, I., and Smirnov, A.: AERONET – a federated instrument network and data archive for aerosol characterization, Remote Sens. Environ., 66, 1–16, 1998.

Hoose, C. and Möhler, O.: Heterogeneous ice nucleation on atmospheric aerosols: a review of results from laboratory experiments. Atmos. Chem. Phys., 12, 9817–9854, 2012. doi:10.5194/acp-12-9817-2012

Hu, Q., Goloub, P., Veselovskii, I., Bravo-Aranda, J.-A., Popovici, I. E., Podvin, T., Haeffelin, M., Lopatin, A., Dubovik, O., Pietras, C., Huang, X., Torres, B., and Chen, C.: Long-range-transported Canadian smoke plumes in the lower stratosphere over northern France, Atmos. Chem. Phys., 19, 1173-1193, 2019. https://doi.org/10.5194/acp-19-1173-2019.

453 Jahl, L. G., Brubaker, T. A., Polen, M. J., Jahn, L. G., Cain, K. P., Bowers, B. B., Fahy, W. D.,

454   Graves, S., and Sullivan, R. C.: Atmospheric aging enhances the ice nucleation ability of

455   biomass-burning aerosol, Science Advances, 7, eabd3440, 2021.

456 Kanji, Z. A., Ladino, L. A., Wex, H., Boose, Y., Burkert-Kohn, M., Cziczo, D. J., and Krämer,

457   M.: Chapter 1: Overview of ice nucleating particles, Meteor Monogr., Am. Meteorol. Soc., 58,

458   1.1-1.33, https://doi.org/10.1175/amsmonographs-d-16-0006.1, 2017.

459 Khaykin, S., Legras, B., Bucci, S., Sellitto, P., Isaksen, L., Tencé, F., Bekki, S., Bourassa, A.,

460   Rieger, L., Tawada, D., Jumelet, J., and Godin-Beekmann, S.: The 2019/20 Australian wildfires

461   generated a persistent smoke-charged vortex rising up to 35 km altitude, Commun. Earth

462   Environ., 1, 22, https://doi.org/10.1038/s43247-020-00022-5, 2020.

463 Klett J.D., "Lidar inversion with variable backscatter/extinction ratios", Appl.Opt. 24, 1638-1643,

464   1985.

465 Knopf, D. A., Alpert, P. A., and Wang, B.: The role of organic aerosol in atmospheric ice

466   nucleation: a review, ACS Earth and Space Chemistry, 2, 168–202, 2018.

467 Müller, D., Wandinger, U., and Ansmann, A.: Microphysical particle parameters from extinction

468   and backscatter lidar data by inversion with regularization: theory, Appl. Opt. 38, 2346-2357,

469   1999.

470 Müller, D., Mattis, I., Wandinger, U., Ansmann, A., Althausen, A., and Stohl, A.: Raman lidar

471   observations of aged Siberian and Canadian forest fire smoke in the free troposphere over

472   Germany in 2003: Microphysical particle characterization, J. Geophys. Res., 110, D17201,

473   doi:10.1029/2004JD005756, 2005.

474 Murray, B. J., O'Sullivan, D., Atkinson, J. D., and Webb, M. E.: Ice nucleation by particles

475   immersed in supercooled cloud droplets, Chem. Soc. Rev., 41, 6519–6554,

476   https://doi.org/10.1039/c2cs35200a, 2012.

477 Ohneiser, K., Ansmann, A., Engelmann, R., Ritter, C., Chudnovsky, A., Veselovskii, I., Baars, H.,

478   Gebauer, H., Griesche, H., Radenz, M., Hofer, J., Althausen, D., Dahlke, S., and Maturilli, M.:

479   Siberian fire smoke in the High-Arctic winter stratosphere observed during MOSAiC 2019–

480   2020, Atmos. Chem. Phys. Discuss. [preprint], https://doi.org/10.5194/acp-2021-117, in

481   review, 2021.

482 Peterson, D. A., Campbell, J. R., Hyer, E. J., Fromm, M. D., Kablick, G. P., Cossuth, J. H., and
483   DeLand, M. T.: Wildfire-driven thunderstorms cause a volcano-like stratospheric injection of
484   smoke, npj Clim. Atmos. Sci., 1, 30, https://doi.org/10.1038/s41612-018-0039-3, 2018

485 Pérez-Ramírez, D., Whiteman, D. N., Veselovskii, I., Kolgotin, A., Korenskiy, M., and Alados-
486   Arboledas, L.: Effects of systematic and random errors on the retrieval of particle
487   microphysical properties from multiwavelength lidar measurements using inversion with
488   regularization, Atmos. Meas. Tech., 6, 3039-3054, 2013.

489 Prata, A.T., Young, S.A., Siems S.T., and Manton, M.J.: Lidar ratios of stratospheric volcanic ash
490   and sulfate aerosols retrieved from CALIOP measurements Atmos. Chem. Phys., 17, 8599–
491   8618, 2017. https://doi.org/10.5194/acp-17-8599-2017

492 Reichardt, J., Leinweber, R., Schwebe, A.: Fluorescing aerosols and clouds: investigations of co-
493   existence, Proceedings of the 28th ILRC, Bucharest, Romania, 25-30 June, 2017.

494 Richardson, S.C., Mytilinaios, M., Foskinis, R., Kyrou, C., Papayannis, A., Pyrri, I., Giannoutsou,
495   E., Adamakis, I.D.S.: Bioaerosol detection over Athens, Greece using the laser induced
496   fluorescence technique, Science of the Total Environment 696, 133906, 2019.
497   https://doi.org/10.1016/j.scitotenv.2019.133906

498 Schrod, J., Weber, D., Drücke, J., Keleshis, C., Pikridas, 5 M., Ebert, M., Cvetkovic´, B., Nickovic,
499   S., Marinou, E., Baars, H., Ansmann, A., Vrekoussis, M., Mihalopoulos, N., Sciare, J., Curtius,
500   J., and Bingemer, H. G.: Ice nucleating particles over the Eastern Mediterranean measured by
501   unmanned aircraft systems, Atmos. Chem. Phys., 17, 4817-4835, https://doi.org/10.5194/acp-
502   17-4817-2017, 2017.

503 Sullivan, S. C., Morales Betancourt, R., Barahona, D., and Nenes, A.: Understanding cirrus ice
504   crystal number variability for different heterogeneous ice nucleation spectra, Atmos. Chem.
505   Phys., 16, 2611–2629, https://doi.org/10.5194/acp-16-2611-2016, 2016.

506 Umo, N. S., Murray, B. J., Baeza-Romero, M. T., Jones, J. M., Lea-Langton, A. R., Malkin, T.
507   L., O'Sullivan, D., Neve, L., Plane, J. M. C., and Williams, A.: Ice nucleation by combustion
508   ash particles at conditions relevant to mixed-phase clouds, Atmospheric Chemistry and
509   Physics, 15, 5195–5210, https://doi.org/10.5194/acp-15-5195-2015,

510 Venable, D. D., Whiteman, D. N., Calhoun, M. N., Dirisu, A.O., Connell, R. M., Landulfo, E.:
511   Lamp mapping technique for independent determination of the water vapor mixing ratio
512   calibration factor for a Raman lidar system, Appl. Opt., 50, 4622 - 4632, 2011.

513   Veselovskii I., Kolgotin, A., Griaznov, V., Müller, D., Wandinger, U., Whiteman, D.: Inversion

514   with regularization for the retrieval of tropospheric aerosol parameters from multi-wavelength

515   lidar sounding, Appl.Opt. 41, 3685-3699, 2002.

516   Veselovskii, I., Whiteman, D. N., Korenskiy, M., Suvorina, A., Kolgotin, A., Lyapustin, A., Wang,

517   Y., Chin, M., Bian, H., Kucsera, T. L., Pérez-Ramírez, D., and Holben, B.: Characterization of

518   forest fire smoke event near Washington, DC in summer 2013 with multiwavelength lidar,

519   Atmos. Chem. Phys., 15, 1647-1660, https://doi.org/10.5194/acp-15-1647-2015, 2015.

520   Veselovskii, I., Hu, Q., Goloub, P., Podvin, T., Korenskiy, M., Pujol, O., Dubovik, O., Lopatin,

521   A.: Combined use of Mie-Raman and fluorescence lidar observations for improving aerosol

522   characterization: feasibility experiment, Atm. Meas. Tech., 13, 6691–6701, 2020.

523   doi.org/10.5194/amt-13-6691-2020.

524   Veselovskii, I., Hu, Q., Goloub, P., Podvin, T., Choël, M., Visez, N., and Korenskiy, M.: Mie–

525   Raman–fluorescence lidar observations of aerosols during pollen season in the north of France,

526   Atm. Meas. Tech., 14, 4773–4786, 2021. doi.org/10.5194/amt-14-4773-2021

527

528 Table 1. Conversion factors C_N, C_S, and C_V, and fluorescence capacity G_F at height H for five
529 smoke episodes. Volume and surface area concentration of smoke particles, obtained by the
530 inversion of $3\beta+2\alpha$ lidar observations (V, S), are given together with values calculated from
531 fluorescence measurements (V^S, S^S) and using conversion factors (Eq. 4).

Date dd/mm/yy	H, km	C_N, $10^4 \frac{cm^{-3}}{Mm^{-1}sr^{-1}}$	C_S, $10^4 \frac{\mu m^2 cm^{-3}}{Mm^{-1}sr^{-1}}$	C_V, $10^4 \frac{\mu m^3 cm^{-3}}{Mm^{-1}sr^{-1}}$	G_F, 10^{-4}	V, μm^3/cm^3		S, μm^2/cm^3	
						V	V^S	S	S^S
23/06/20	4.9	88	35	2.4	3.5	21±4	19±4	306±75	237±60
11/09/20	7.5	75	28	2.0	3.9	7.6±1.6	8.7±1.6	111±25	111±25
14/09/20	6.0	90	34	2.3	3.7	6.4±1.3	6.1±1.3	94±25	78±20
17/09/20	6.8	21	21	2.3	2.9	8.0±1.6	7.8±1.6	73±18	100±25
20/09/20	4.9	33	22	2.0	4.3	2.7±0.5	2.9±0.6	31±8	37±9

532
533
534
535
536
537 Table 2. Number N^S, surface area S^S, and volume V^S concentrations of smoke particles inside the
538 ice cloud at height H estimated from fluorescence measurements by applying the conversion
539 factors in Eq. (4) for four measurement sessions.

Date dd/mm/yy	Time UTC	H, km	β_F, 10^{-4} Mm^{-1}sr^{-1}	N^S, cm^{-3}	S^S, μm^2/cm^3	V^S, μm^3/cm^3
12/09/20	01:20-01:45	10.5	0.32	20±10	9±2.3	0.7±0.15
12-13/09/20	21:00-03:00	12.5	0.06	3.5±1.8	1.6±0.4	0.13±0.03
17/09/20	22:45-23:45	8.5	6.5	400±200	180±45	14±3
24-25/11/20	18:00-06:00	8.0	0.013	0.8±0.4	0.36±0.09	0.03±0.006

540
541

542   **Appendix A.** Estimation of smoke parameters from Mie-Raman and fluorescence lidar

543   measurements.
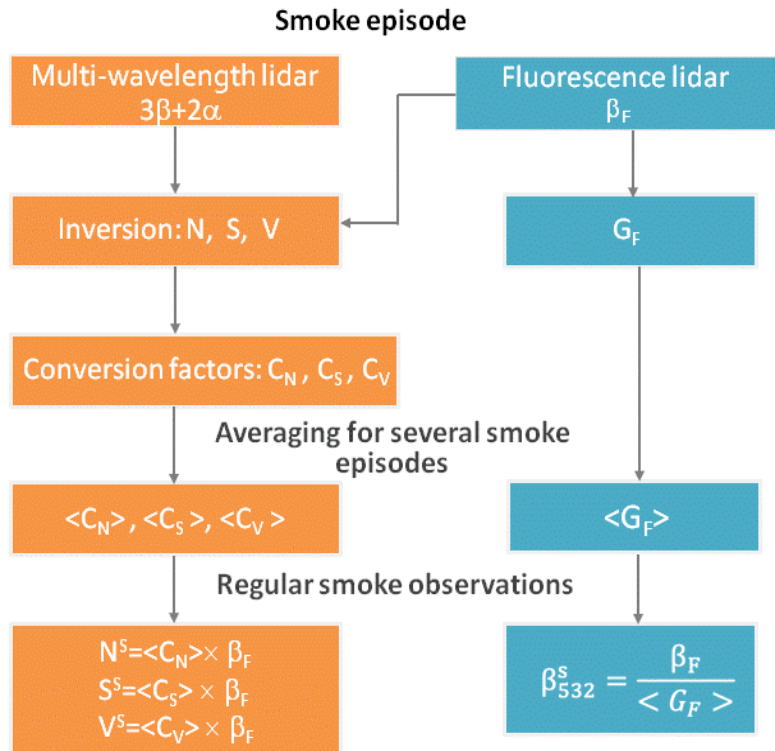
544

545   Fig.A. Flow chart showing the main steps of the procedure of smoke parameters estimation from

546   multiwavelength Mie-Raman and fluorescence lidar measurements. Procedure includes the

547   following steps. (i) For a strong smoke layer the $3\beta+2\alpha$ data set, derived from multiwavelength

548   Mie-Raman lidar observations, is inverted to the particle number N, surface S and volume V

549   density. (ii) Conversion factors C_N, C_S, C_V are calculated from Eq.(3) by using the fluorescence

550   backscattering coefficient β_F. (iii) Different smoke events are analyzed to get mean values of

551   conversion factors $<C_N>$, $<C_S>$, $<C_V>$. These mean values are used to estimate smoke

552   concentration in weak layers in UTLS and inside cirrus clouds in regular observations. The mean

553   value of smoke fluorescence capacity $<G_F>$ allows estimation of smoke contribution β^s_{532} to the

554   total backscattering coefficient β_{532}.

555
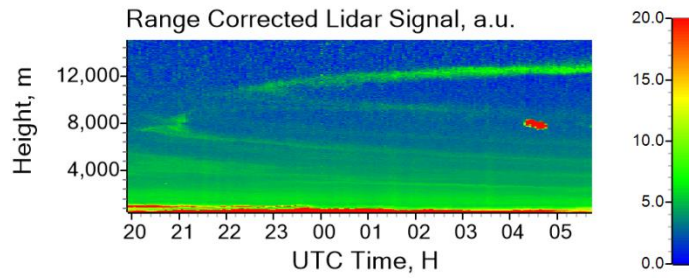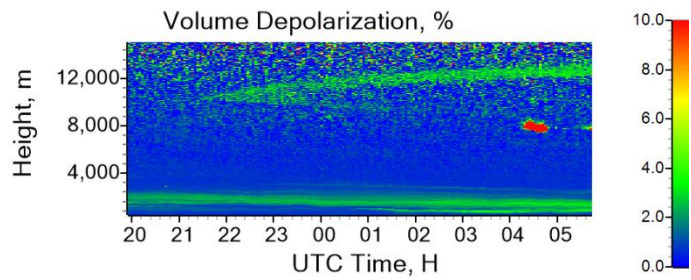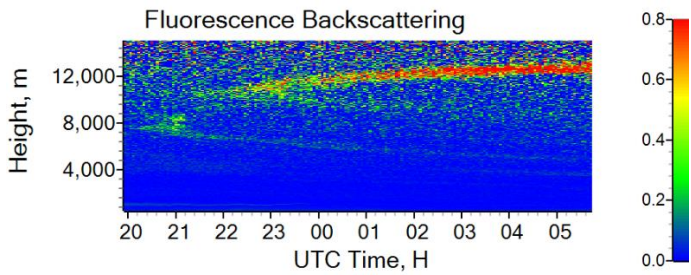
Fig.1. Range corrected lidar signal at 1064 nm, volume depolarization ratio at 1064 nm and fluorescence backscattering coefficient (in 10^{-4} $Mm^{-1}sr^{-1}$) on 4-5 November 2020.

564

565
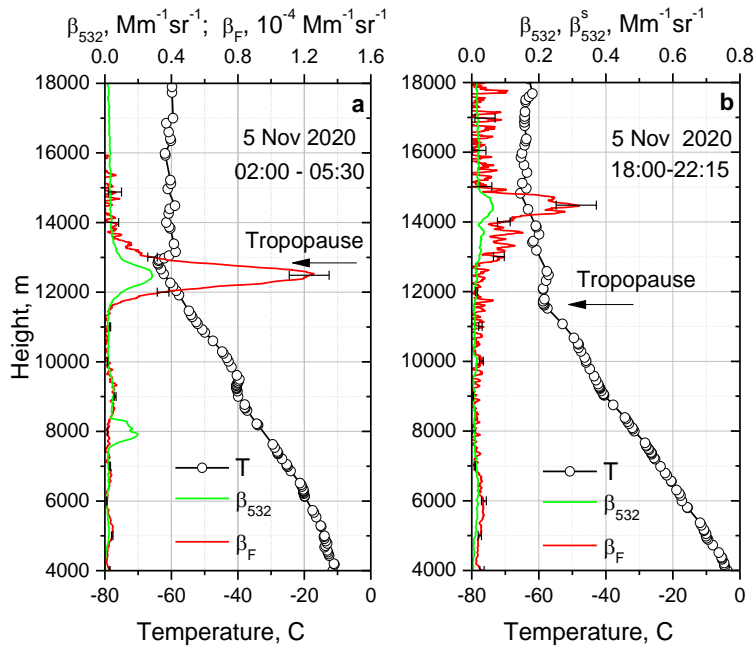
566 Fig.2. Vertical profiles of aerosol backscattering β_{532} and fluorescence backscattering β_F
567 coefficients on 5 November 2020 for the periods (a) 02:00 - 5:30 UTC and (b) 18:00 – 22:15 UTC.
568 Open symbols show the temperature profile measured by the radiosonde launched at
569 Herstmonceux (UK).

570

571

572
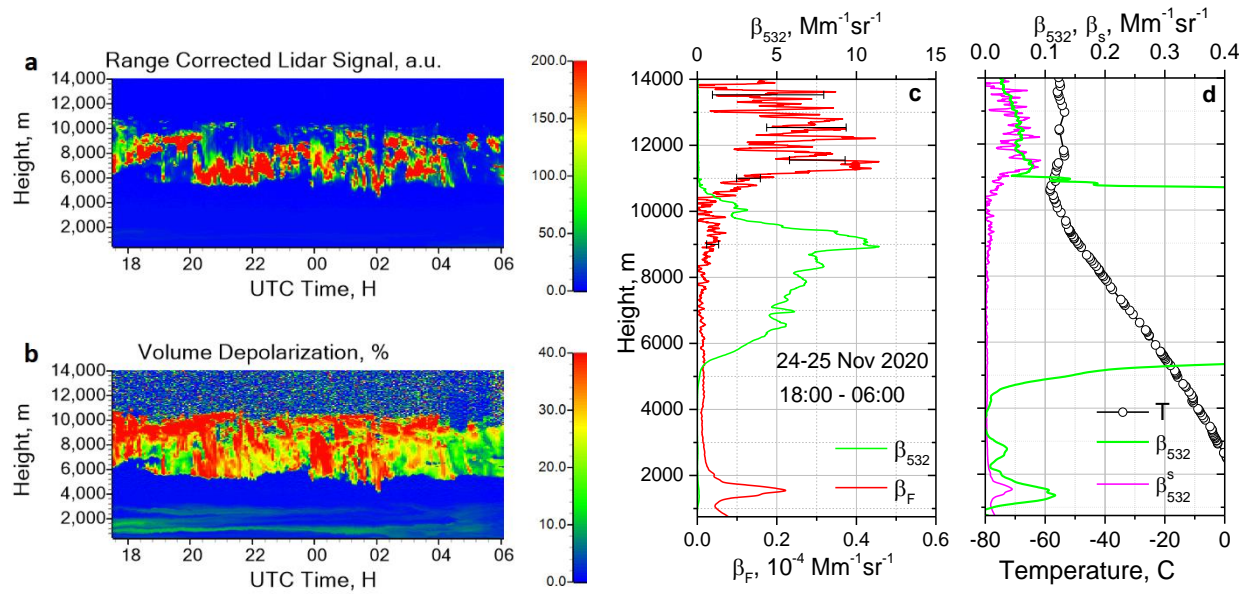
573   Fig.3. Smoke fluorescence in the presence of clouds on 24 – 25 November 2020. (a, b)
574   Spatiotemporal variations of the range corrected lidar signal and volume depolarization at 1064
575   nm. (c) Vertical profiles of the aerosol β_{532} and fluorescence β_F backscattering coefficients. (d)
576   Aerosol backscattering β_{532} together with smoke backscattering β_{532}^{s} coefficient, computed from
577   β_F for $G_F=4.5\times10^{-4}$. Open symbols show temperature profile measured by the radiosonde at
578   Herstmonceux.
579
580
581

582
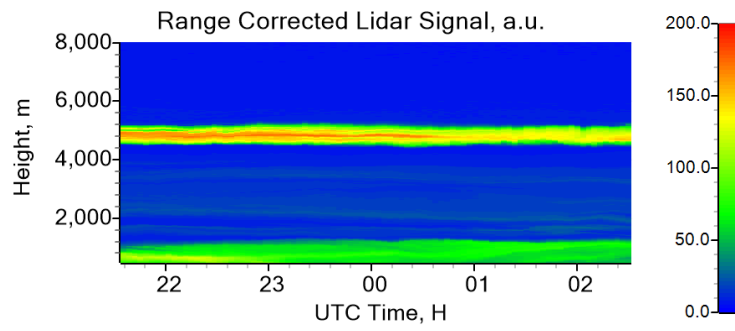
583
584   Fig.4. Range corrected lidar signal at 1064 nm on 23-24 June 2020, revealing a smoke layer
585   between 4500 and 5200 m height.
586
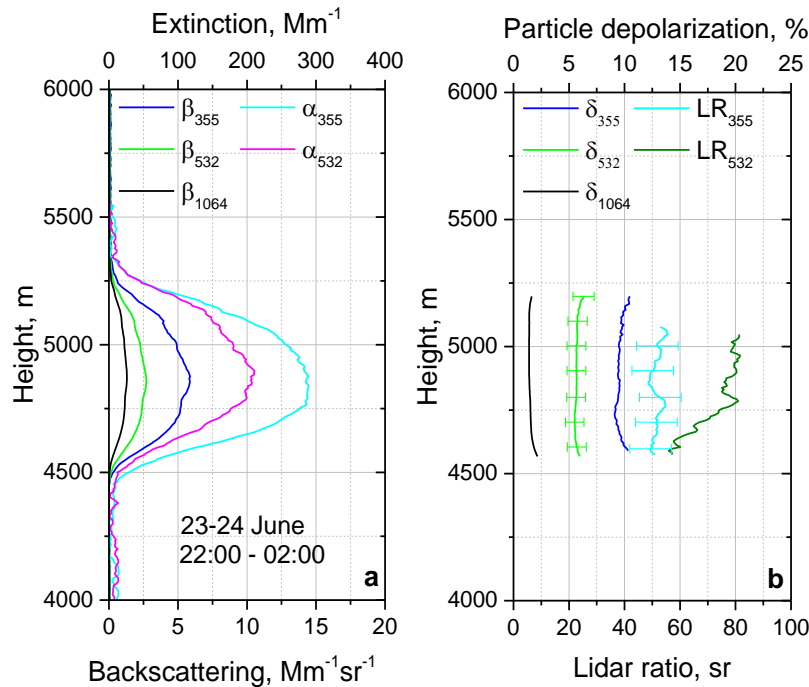
587
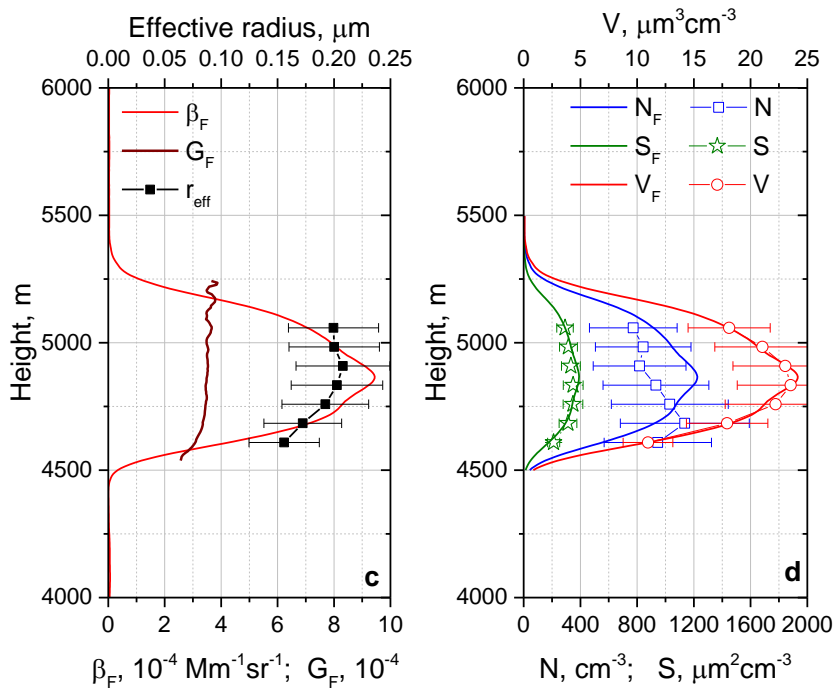
588
589
590 Fig.5. Smoke layer on 23-24 June 2020. (a) Vertical profiles of backscattering (β_{355}, β_{532}, β_{1064})
591 and extinction (α_{355}, α_{532}) coefficients. (b) Particle depolarization ratios (δ_{355}, δ_{532}, δ_{1064}) and lidar
592 ratios (LR$_{355}$, LR$_{532}$). (c) Fluorescence backscattering (β_F), fluorescence capacity (G_F) and the
593 particle effective radius (r_{eff}). (d) Number (N, N_F), surface area (S, S_F) and volume (V, V_F)
594 concentrations obtained by inversion of 3β+2α observations (symbols) and calculated from the
595 fluorescence backscattering (lines) by using the mean conversion factors defined in Eq. (3).
596
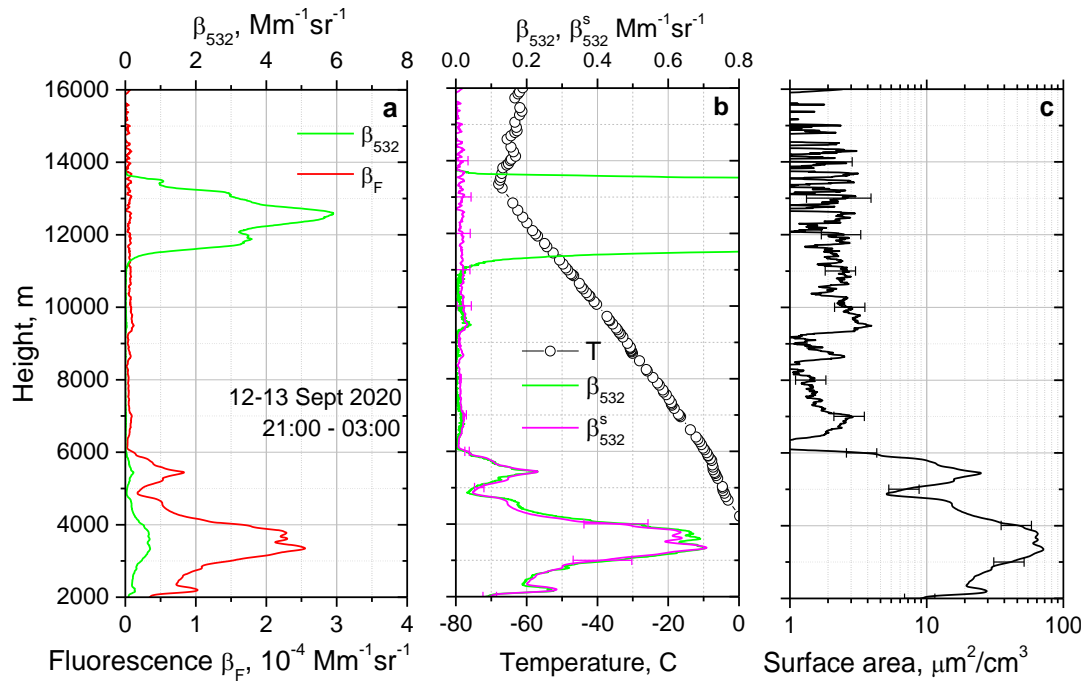
597   Fig.6.

598 Observation of smoke fluorescence on 12-13 September 2020, 21:00 – 03:00 UTC. (a) Vertical

599 profiles of the aerosol backscattering β_{532} and fluorescence backscattering β_F coefficients. (b)

600 Aerosol backscattering β_{532} together with smoke backscattering β^s_{532} coefficient computed from

601 β_F for $G_F=3.6\times10^{-4}$. (c) Surface area concentration of the smoke particles calculated from β_F by

602 using the respective conversion factor from (4). Open symbols show the temperature profile

603 measured by the radiosonde at Herstmonceux.

604

605

606

607
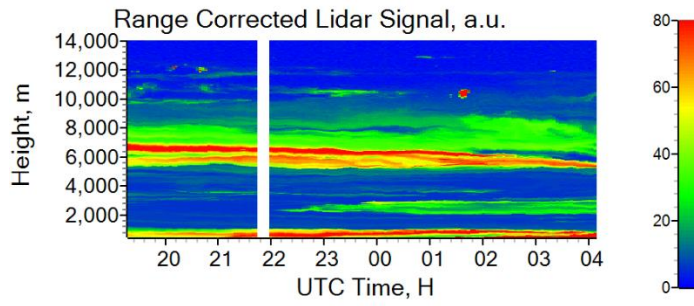
608
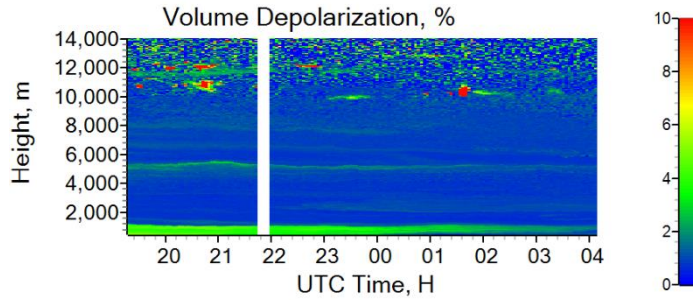
609
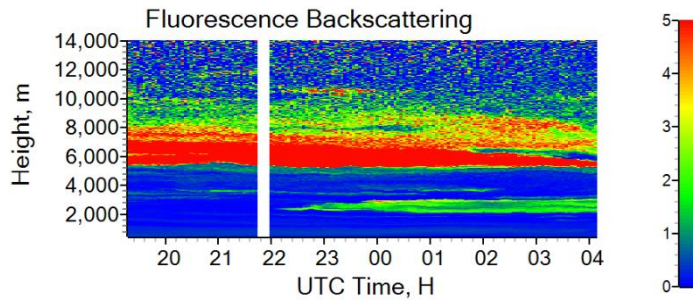
610
611 Fig.7. Formation of ice particles at heights above 10 km inside a smoke layer on 11-12 September 2020.
612 Spatiotemporal variations of range corrected lidar signal at 1064 nm, volume depolarization ratio at
613 1064 nm and fluorescence backscattering coefficient (in 10^{-4} $Mm^{-1}sr^{-1}$).
614
615

616
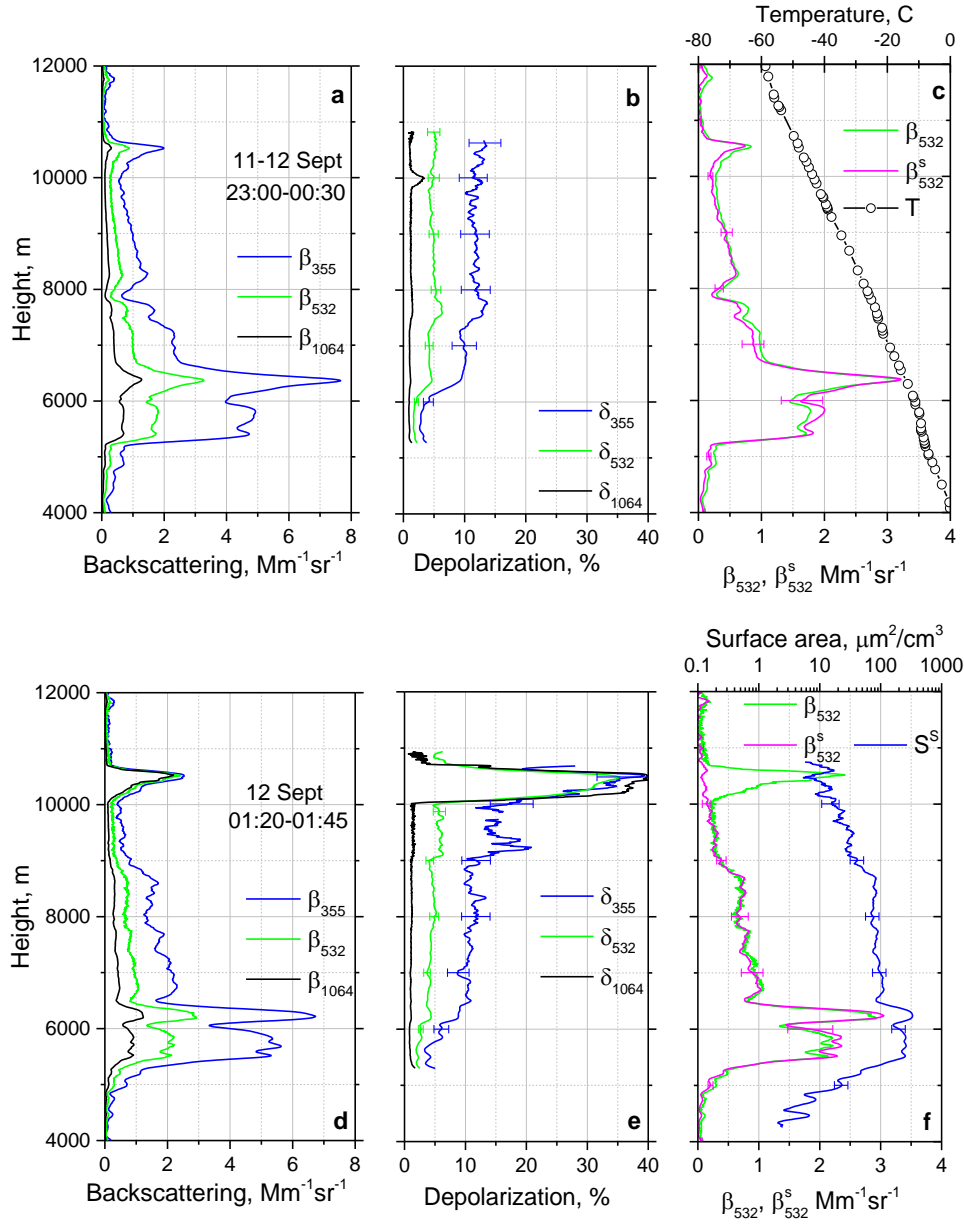
617
618 Fig.8. Formation of ice particles at 10-11 km height inside a smoke layer on 11-12 September
619 2020. Vertical profiles of (a, d) the aerosol backscattering coefficients β_{355}, β_{532}, β_{1064}; (b, e) the
620 particle depolarization ratios δ_{355}, δ_{532}, δ_{1064}; (c, f) β_{532} together with backscattering coefficient of
621 smoke β_{532}^{s}, calculated from fluorescence backscattering β_F assuming $G_F=4.0\times10^{-4}$. Plot (f) shows
622 also the smoke surface area concentration S^S of the smoke particles calculated from β_F by applying
623 the respective conversion factor in Eq. (4). Results are given for the time intervals 23:00 – 00:30
624 UTC and 01:20 – 01:45 UTC: prior and during ice cloud formation at 10.5 km height. The
625 temperature profile measured by the radiosonde at Herstmonceux is shown with open symbols in
626 panel (c).

627

628

629

630 Fig.9. Formation of ice particles at heights above 8 km inside the smoke layer on 17-18 September 2020.
631 Spatiotemporal variations of range corrected lidar signal at 1064 nm, volume depolarization ratio at
632 1064 nm and fluorescence backscattering coefficient (in 10^{-4} $Mm^{-1}sr^{-1}$).

633

634

635

636
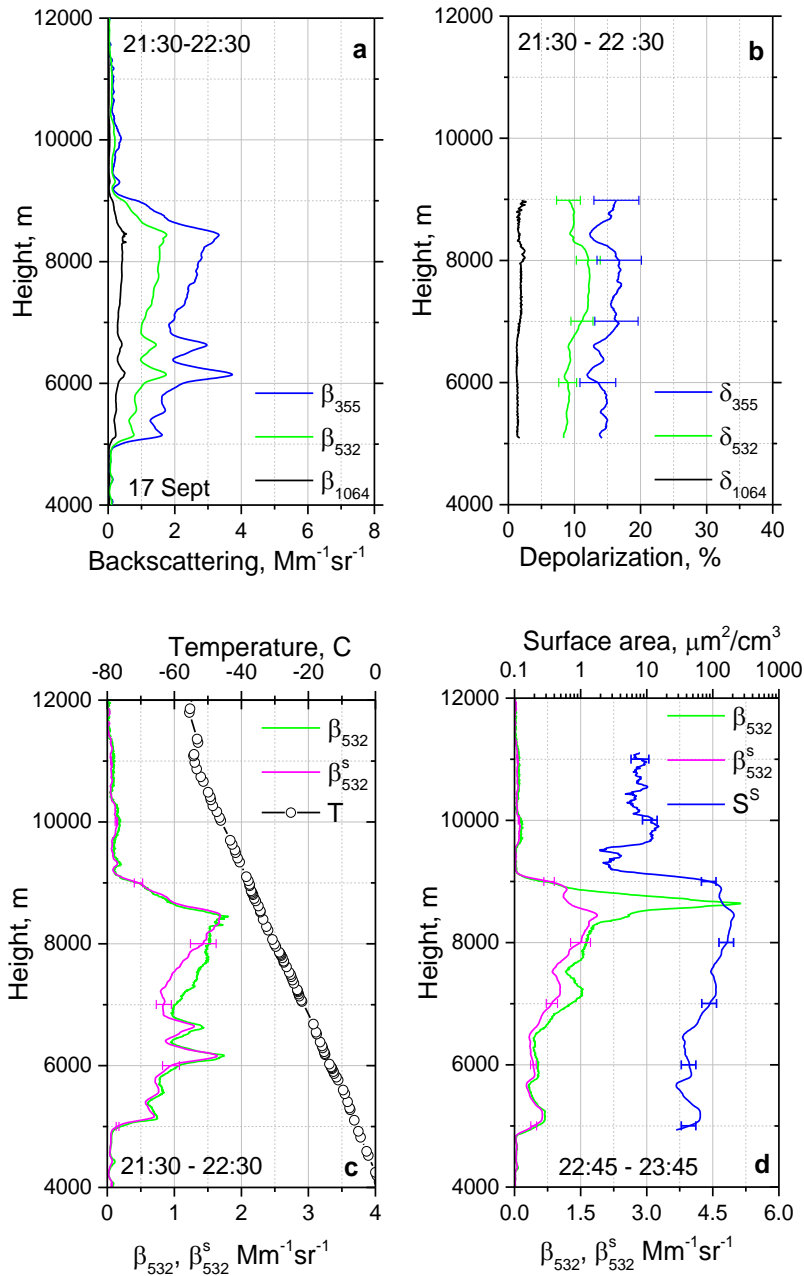
637
638 Fig.10. Formation of ice particles at 8.5-8.6 km height inside a smoke layer on 17 September 2020.
639 Vertical profiles of (a) the aerosol backscattering coefficients β_{355}, β_{532}, β_{1064}; (b) the particle
640 depolarization ratios δ_{355}, δ_{532}, δ_{1064}; (c, d) β_{532} together with backscattering coefficient of smoke
641 β_{532}^{s}, calculated from fluorescence backscattering β_F assuming $G_F=3.5\times10^{-4}$. Results are given for
642 the time intervals (a-c) 21:30 – 22:30 UTC and (d) 22:45 – 23:45 UTC: prior and during ice
643 formation at 8.5 km height. Plot (d) shows also the surface area concentration of the smoke
644 particles calculated from β_F by applying the respective conversion factor from (4). The temperature
645 profile measured by the radiosonde at Herstmonceux is shown with open symbols in panel (c).